Published in final edited form as:
IEEE Trans Image Process. 2007 December ; 16(12): 3005–3019.

Blind Deconvolution of Medical Ultrasound Images: A Parametric Inverse Filtering Approach

Oleg Michailovich [Member, IEEE] and
School of Electrical and Computer Engineering, Georgia Institute of Technology, Atlanta, GA 30332 USA. He is currently with the Department of Electrical and Computer Engineering, University of Waterloo, Waterloo, ON N3L 3G1 Canada (olegm@uwaterloo.ca)

Allen Tannenbaum [Member, IEEE]
School of Electrical and Computer Engineering, Georgia Institute of Technology, Atlanta, GA 30332 USA, and also with the Department of Electrical and Computer Engineering, The Technion—Israel Institute of Technology, Haifa, Israel (tannenba@ece.gatech.edu)

Abstract

The problem of reconstruction of ultrasound images by means of blind deconvolution has long been recognized as one of the central problems in medical ultrasound imaging. In this paper, this problem is addressed via proposing a blind deconvolution method which is innovative in several ways. In particular, the method is based on parametric inverse filtering, whose parameters are optimized using two-stage processing. At the first stage, some partial information on the point spread function is recovered. Subsequently, this information is used to explicitly constrain the spectral shape of the inverse filter. From this perspective, the proposed methodology can be viewed as a "hybridization" of two standard strategies in blind deconvolution, which are based on either concurrent or successive estimation of the point spread function and the image of interest. Moreover, evidence is provided that the "hybrid" approach can outperform the standard ones in a number of important practical cases. Additionally, the present study introduces a different approach to parameterizing the inverse filter. Specifically, we propose to model the inverse transfer function as a member of a principal shift-invariant subspace. It is shown that such a parameterization results in considerably more stable reconstructions as compared to standard parameterization methods. Finally, it is shown how the inverse filters designed in this way can be used to deconvolve the images in a nonblind manner so as to further improve their quality. The usefulness and practicability of all the introduced innovations are proven in a series of both *in silico* and *in vivo* experiments. Finally, it is shown that the proposed deconvolution algorithms are capable of improving the resolution of ultrasound images by factors of 2.24 or 6.52 (as judged by the autocorrelation criterion) depending on the type of regularization method used.

Keywords

Bayesian estimation; blind deconvolution; inverse filtering; PSI subspaces; ultrasound imaging

I. Introduction

Medical ultrasound imaging is currently considered to be on the leading edge in noninvasive diagnostic imaging, whose cost-benefit ratio in terms of accessibility, portability, and safety far exceeds that of alternative technologies. Unfortunately, the advantages of ultrasound

imaging are counterbalanced by the relatively low quality of ultrasound images as compared to other modalities, such as, e.g., X-ray CT or MRI. As a result, significant efforts have been expended in the past few decades to improve the quality of medical ultrasound via both modernizing the design of ultrasound scanners and incorporating effective signal processing schemes in the process of image formation. Among the latter approaches are those based on *deconvolution* techniques [1]-[7], which are in the focus of the present developments.

In ultrasound imaging, the convolution model of image formation implies a linear interaction between the acoustic field and studied tissues. Although such an interaction could only occur on conditions of *weak scattering* [8], which is not ubiquitous in biological tissues, the convolution model has long been known as a good approximation of the real field-tissue interaction. For this reason, this model is chosen as the basis for the present study.

Under the convolution model, the acquired *radio-frequency* (RF) image is considered to be a result of convolution between the *point-spread function* (PSF) of the ultrasound scanner and a *tissue-reflectivity function*. Unfortunately, such a global description can rarely be used to account for the formation of a *whole* RF-image, since, in ultrasound imaging, the PSF happens to exhibit spatial dependency due to the nonuniformity of focusing, diffraction effects, dispersive attenuation, and phase aberrations [9]-[11]. However, relatively low spatial variability of the above phenomena makes it possible to replace the problem of nonstationary deconvolution by a number of stationary deconvolution problems. It is commonly done via dividing the whole RF-image into several (possible overlapping) segments, each of which may be modeled using the stationary convolution model with a different PSF. Note that, in this case, neither the "local" PSF nor the corresponding reflectivity function are known, and, therefore, they should be recovered directly from the data and, hence, the term "blind" [12]. Without any loss of generality, the discussion below is confined to the problem of deconvolution of one (quasi-) stationary image segment, and it is assumed that, having deconvolved all the image segments, the entire image can be recovered via combining all the local results obtained in this manner (as proposed, e.g., in [13]).

In most of the existing methods for blindly deconvolving ultrasound images, the procedures of estimating the PSF and recovering the tissue reflectivity function are disjoint, with the former being a prerequisite stage to the latter. Thus, for example, in [4] and [5], the PSF is estimated based on results from the theory of system identification. Although these approaches may work reliably when applied to 1-D data, their extension to higher dimensions seems to be impractical, as it would require a rather large amount of high-dimensional data to be stored and averaged to derive useful estimates. From this perspective, a more practicable alternative is available within the framework of *homomorphic signal processing* [14, Ch. 11]. In particular, the *cepstrum-based* methods for estimating the PSF [6], [15], [16], as well as their generalizations [7], [17] have been demonstrated to result in estimation algorithms which seem to optimally balance between the estimation accuracy and computational efficiency.

The fundamental assumption underpinning all the homomorphic deconvolution methods is that the log magnitude and phase of the Fourier transform of the PSF can be estimated as smoothed versions of the corresponding quantities of the RF-image. While smoothing the log spectra can be implemented in a straightforward manner, the situation is not that simple with the phases. This is because, in practice, the latter can only be computed in their *principal* form (i.e., *modulo* 2π), which makes the problem of *phase unwrapping* an indispensable part of homomorphic deconvolution [18]. Unfortunately, due to its being ill-posed, the phase unwrapping is known to be a very difficult reconstruction problem [19],

whose solution is rarely error free. Moreover, the assumption of minimum-phase (which could have been used to avoid the phase estimation had the PSF possessed this property) does not seem to be applicable in ultrasound imaging in general [6]. Although there are several other efficient ways to avoid the problem of phase unwrapping [20]-[22], estimation of the Fourier phase of the PSF from that of the RF-image is generally difficult because of the latter being an extremely noisy, nonsmooth, and severely aliased function. Consequently, alternative ways for estimating the PSF should be sought.

A different approach to the problem of blind deconvolution of medical ultrasound images is developed in this paper. The main attribute of the proposed deconvolution method consists in its ability to estimate the tissue reflectivity function using only *partial* information on the PSF, namely, its power spectrum. The latter is assumed to be estimated before the deconvolution process is initiated using the method detailed in [7]. Note that, from this perspective, the proposed method can be viewed as a "hybrid" approach, as it can be ascribed neither to the group of deconvolution techniques which recover the PSF *in full* prior to estimating the reflectivity function, nor to those which recover the PSF and the reflectivity function concurrently [23], [24].

The deconvolution method described here is based on the concept of *inverse filtering* as in [12] and [24]. Specifically, the inverse transfer function is modeled as a member of a periodic, *principal shift-invariant* subspace [25], [26]. This kind of modeling presents a novel and very versatile way to design the inverse filter response, which allows one to perform the inversion in a considerably more stable and efficient manner as compared to the methods based on standard parameterization. Moreover, it is shown that the inverse filters constructed in this way can be used to estimate the PSF, followed by deconvolving the ultrasound images in a *nonblind* manner using the *maximum a posteriori* (MAP) estimation framework. It is demonstrated via a series of both *silico* and *in vivo* experiments that the latter deconvolution strategy may result in solutions of higher resolution and contrast as compared to those obtained via inverse filtering.

The paper is organized as follows. Section II provides a formal definition of the convolution model and of inverse filtering. Section III briefly describes the method used for estimating the power spectrum of the PSF, whereas Section IV details the optimization procedure, by means of which the reflectivity function is recovered. In Section V, a novel approach to parameterizing the inverse filter is introduced. Some essential details which are necessary for numerical implementation of the proposed algorithm are given in Section VI. The relation of the proposed inverse filtering to nonblind deconvolution methods is discussed in Section VII, while experimental results are summarized in Section VIII. Section IX concludes the paper with a discussion, and some directions for future research.

II. Image Reconstruction Via Inverse Filtering

In this study, instead of real-valued RF-images, we work with complex *in phase/quadrature* (IQ) images, which are obtained from the former via the process of frequency demodulation. Since the frequency demodulation is normally followed by anti-aliasing filtering and downsampling, working with IQ images is advantageous due to their higher signal-to-noise ratio (SNR) and smaller size. Moreover, due to the linearity of the demodulation process, the convolution model can be used to describe the formation of IQ-images, as well. In particular, denoting by $g(\mathbf{n})$,$h(\mathbf{n})$, and $f(\mathbf{n})$ the IQ-image, the complex PSF, and the complex reflectivity function, respectively, the image formation model is given by

$$g(\mathbf{n}) = h(\mathbf{n}) * f(\mathbf{n}) + u(\mathbf{n}), \quad (1)$$

Here, $\mathbf{n} \in \mathbb{Z}^d$ is an integer, d-dimensional vector that indexes the data samples, the asterisk stands for the convolution operator, and the term $u(\mathbf{n})$ is added to account for measurement noise, as well as for all possible phenomena which are not accounted for by the convolution model. Alternatively, the model (1) can be specified in the Fourier domain by applying the discrete Fourier transform (DFT) to both its sides. In this case, (1) becomes

$$G(w) = H(w)F(w) + U(w) \quad (2)$$

with the upper-case letters in (2) denoting the DFT of their lower-case counterparts in (1) (Note that by the DFT of a sequence $x(\mathbf{n})$, we mean the trigonometric series $X(\boldsymbol{\omega}) = \Sigma_{\mathbf{n}} x(\mathbf{n})\exp\{-i(\mathbf{n} \cdot \omega)\}$, where the "dot" denotes the Euclidean inner product). Due to their periodicity, the functions in (2) can be defined on the d-dimensional torus $\mathbb{T}^d = [\mathbb{R}/2\pi\mathbb{Z}]^d$ (which we usually understand to be $\mathbb{R}^d$ with the identification of points modulo 2π).

The convolution of the tissue-reflectivity function with the band-limited PSF results in an attenuation (or even complete suppression) of some spectral components of the former. These attenuated components can be recovered though the process of *inverse filtering*

$$f(\mathbf{n}) \simeq s(\mathbf{n}) * g(\mathbf{n}) \quad (3)$$

where $s(\mathbf{n})$ is commonly referred to as a *deconvolution kernel* or *inverse filter*. Note that, because of the scale and linear-phase ambiguity problem, which is inherent in deconvolution, (3) is not general and should be replaced by $s(\mathbf{n})*g(\mathbf{n}) \simeq \alpha f(\mathbf{n}-\mathbf{n}_0)$ with α being an arbitrary scalar and $\mathbf{n}_0$ designating an arbitrary translation of the estimate. However, in order to simplify the notation, the relation (3) is used throughout the text, while the more general case is tacitly implied.

To estimate $f(\mathbf{n})$ according to (3), an optimal value of the inverse filter has to be found first. In the current study, the design of the inverse filter is implemented in the domain of its DFT. Specifically, let Γ be a finite set of indices. Subsequently, given a predefined set of basis functions, $\{\Psi_k(\boldsymbol{\omega})\}_{k\in\Gamma}$, the DFT $S(\boldsymbol{\omega})$ of the inverse filter $s(\mathbf{n})$ is sought in the following *parametric* form:

$$S(\omega) = S(\omega|\theta) = \sum_{k\in\Gamma} \theta_k \Psi_k(w) \quad (4)$$

with $\boldsymbol{\theta} \equiv \{\theta_k\}_{k\in\Gamma}$ being a set of the filter parameters. Note that, in general, both functions $\Psi_k(\boldsymbol{\omega})$ and parameters θ_k are complex. In the sections that follow, we will show that the representation by (4) is very general, since it accommodates some standard filter designs, while allowing a number of substantial developments.

III. Partial Estimation of the PSF

As was noted in the Introduction, because of its "hybrid" nature, the proposed deconvolution algorithm is implemented in two stages. At the first stage, the magnitude of the DFT of the PSF is estimated using the method described in [7]. The latter takes advantage of the linear relationship between the log spectra of the IQ-image, the PSF, and the reflectivity function, which suggests that

$$\log |G(\omega)| \simeq \log|H(\omega)| + \log|F(\omega)| \quad (5)$$

with the noise being ignored for the sake of simplicity. Since $\log|H(\boldsymbol{\omega})|$ is typically a much smoother function as compared to $\log|F(\boldsymbol{\omega})|$, it can be recovered from $\log|G(\boldsymbol{\omega})|$ by means of properly formulated *smoothing* procedure.

The above idea constitutes the basis for cepstrum-based methods of estimating the PSF, in which log $H(\omega)$| is recovered through *linearly filtering* the log spectrum log $G(\omega)$| [14], [6], [15], [16]. Yet, an even more accurate estimation is possible, if the problem of recovering the log magnitude log $|H(\omega)|$ is addressed using the theory of Bayesian estimation [27], as was first proposed in [7] and [17]. In particular, it was proposed in these works that one could reconstruct log $|H(\omega)|$ by subjecting log$|G(\omega)$ to the procedure of *outlier-resistant wavelet de-noising*. It was shown that, as compared with the cepstrum-based estimation, this variant of the wavelet de-noising results in considerably smaller estimation errors, while its complexity barely exceeds that of the linear filtering. For this reason, the method of [7] is employed in the present study for recovering log $|H(\omega)$ or, equivalently, $|H(\omega)|$.

It should be noted that the convolution model also implies that, in the noise-free case, the Fourier phase $\angle G(\omega)$ is equal to the sum of the phases $\angle H(\omega)$ and $\angle F(\omega)$. This fact suggests the possibility to estimate the phase $\angle H(\omega)$ via rejecting the "noise" $\angle F(\omega)$. However, as opposed to the case of Fourier magnitudes, such estimation is much more difficult and usually less successful because of the sizable errors caused by aliasing, as well as by the imperfections of phase unwrapping. In order to overcome the difficulties related to estimating the Fourier phase of the PSF, in this paper, we propose a way to estimate the inverse filter $S(\omega)$ using an estimate $\widehat{H}(\omega)$ of the amplitude $|H(\omega)|$ alone. It is important to note that, having estimated the inverse filter, the latter can be used to estimate the PSF according to

$$H(\omega) \simeq \widehat{H}(\omega) \exp(-i\angle S(\omega)) \quad (6)$$

due to the linearity of inverse filtering.

IV. Estimation of the Inverse Filter

A. Constraining the Power Spectrum of the Inverse Filter

In the case of *parametric inverse filtering*, estimating the inverse filter $S(\omega\,\theta)$ is accomplished via estimating the vector of its parameters θ. In this paper, this estimation scheme is performed subject to a few "design" constraints, the first of which is imposed on the amplitude of $S(\omega|\theta)$. Specifically, given an estimate $|\widehat{H}(\omega)|$ of the DFT amplitude of the PSF, the DFT amplitude of the combined response $S(\omega|\theta)\widehat{H}(\omega)$ is required to be as close to *unity* as possible over the transducer passband. Formally, the parameters of the inverse filter are required to minimize the following functional:

$$E_1(\theta) = \int_{\mathbb{T}^d} \eta\left(|S(\omega|\theta)\widehat{H}(\omega)|^2 - 1\right) d\mu(\omega). \quad (7)$$

Here, $\eta:\mathbb{R} \to \mathbb{R}$ is a convex, lower semicontinuous function that, in fact, defines a norm by means of which the distance between the power spectrum of the combined response and the unity is measured. In this paper, we choose it to be the absolute value function, i.e., $\eta(x) \equiv |x|$, because of the robustness of the resulting norm. For computational reasons, however, it is preferred to use a smooth approximation of the absolute value function, which could be defined, e.g., as

$$\eta(x) = |x/c| - \log(1+|x/c|) \quad (8)$$

with $c \in (0,1]$ being a proximity parameter satisfying $\eta(x) \to |x|$ as $c \to 0^+$. Note that, throughout the experimental stage of this study, this parameter was set to be equal to 0.01.

The measure $d\mu(\boldsymbol{\omega})$ in (7) is a Lebesgue measure, which is intended to "weight" the domain of integration. Such a "weighting" is necessary to guarantee the well-posedness of minimizing $E_1(\boldsymbol{\theta})$. Indeed, in the case when $H(\boldsymbol{\omega})$ converges to zero near the boundary of $\mathbb{T}^d$, a zero weight should be given there to the integrand so as to prevent the resulting inverse filter from becoming unbounded.

B. Statistical Modeliing of the Reflectivity Function

It goes without saying that *unconstrained* minimization of the functional $E_1(\boldsymbol{\theta})$ is pointless, since it admits an infinite number of local minima by virtue of its being "phase-insensitive." In order to overcome this deficiency, we supplement the functional (7) by an additional term which stems from a *likelihood model* of the tissue reflectivity function. In particular, the samples of the latter are assumed to be independently and identically distributed (*i.i.d.*) according to a *non-Gaussian* probability law [5].

At this point, it should be noted that, for the case when the tissue under investigation is composed of diffusive scatterers (e.g., tissue fibers, diminutive aggregates of individual cells, etc.) superimposed on a scanty structure of a few strong specular reflectors (e.g., liver arterioles, organ boundaries, etc.), the corresponding tissue reflectivity function is likely to be a *sparse* sequence [28]. Such a behavior of the reflectivity function can be effectively described using a Laplacian distribution, as it has long been done in numerous applications in signal processing [29]-[32]. Note that, in the field of ultrasound imaging, this assumption seems to have first been advocated in [33].

Assuming that the samples of $f(\mathbf{n})$ are *i.i.d.* copies of a Laplacian random variable, it is straightforward to show that maximizing the *log likelihood* of $f(\mathbf{n})$ amounts to minimizing its ℓ_1-norm. Consequently, we subject the design of our parametric inverse filter to the additional constraint that forces it to recover the most likely configuration of the reflectivity function by minimizing the ℓ_1-norm of its estimate given by

$$E_2(\theta) = \|\mathscr{F}^{-1}\{S(\omega \quad \theta)G(\omega)\}\|_1 \quad (9)$$

where $\mathscr{F}^{-1}$ denotes the *inverse* DFT. Consequently, combining the functionals (7) and (9), the final criterion for estimating the optimal parameters $\boldsymbol{\theta}_{\text{opt}}$ of the inverse filter is defined to be

$$\theta_{\text{opt}} = \arg\min_{\theta} E(\theta) \quad (10)$$

where

$$\begin{aligned} E(\theta) = {} & E_1(\theta) + \lambda E_2(\theta) \\ = {} & \int_{\mathbb{T}^d} \eta\left(|S(\omega\theta)\widehat{H}(w)^2 - 1\right) d\mu(\omega) \\ & + \lambda \|\mathscr{F}^{-1}\{S(\omega\theta)G(\omega)\|_1 \end{aligned} \quad (11)$$

with $\lambda > 0$ being a design parameter which controls the balance between the two optimization terms in (11).

Alternatively to (10) and (11), one can formally define the *maximum-likelihood* (ML) estimate of $\boldsymbol{\theta}$ as a maximizer of the joint probability density of the samples of $\mathscr{F}^{-1}\{S(\omega \quad \theta)G(\omega)\}$. Under the Laplacian model, the ML estimation amounts to minimizing [34]

$$E(\theta) = -\int_{\mathbb{T}^d} \log S(\omega|\theta)\, d\omega + \lambda \| \mathcal{F}^{-1}\{S(\omega\theta)\, G(\omega)\} \|_1. \quad (12)$$

The formal ML approach, however, seems to have a flaw in the case of band-limited PSF, as it explicitly requires the convolution with the PSF to be *invertible*. In particular, the term $-\int_{\mathbb{T}^d} \log|S(\omega|\theta)|\, d\omega$ may be made arbitrary small by increasing the values of $S(\boldsymbol{\omega}|\boldsymbol{\theta})$, which is likely to take place outside of the transducer passband, where the values of $H(\boldsymbol{\omega})$ are relatively small and, as a result, $G(\boldsymbol{\omega})$ is dominated by noises. Consequently, the resulting estimates of the reflectivity function may not be reliable.

C. Sparsity as a "Facilitator" of Optimality

To understand how the sparsity constraint (as it is enforced through minimizing the ℓ_1-norm of $f(\mathbf{n})$) contributes to the convergence of the inverse filter to its optimal form, let us assume for a moment that the noise term in (1) is negligible and the convolution with $h(\mathbf{n})$ is invertible. Then, knowing the Fourier magnitude $|H(\boldsymbol{\omega})|$ of the PSF $h(\mathbf{n})$ implies the possibility to recover the true reflectivity function up to a *phase error*. Alternatively, one can say that, in this case, the reflectivity function $f(\mathbf{n})$ can be recovered up to convolution with an arbitrary sequence $z(\mathbf{n})$ of unit ℓ_1-norm, so that the resulting estimate is given by

$$y(\mathbf{n}) = f(\mathbf{n}) * z(\mathbf{n}) = \sum_k f(\mathrm{k})\, z(\mathrm{k}-\mathrm{n}). \quad (13)$$

Hence, one can see that, in the case when the phase of $S(\boldsymbol{\omega})$ is incorrectly defined, each sample of the estimate $y(\mathbf{n})$ of the reflectivity function is given by a linear combination of the samples of the true reflectivity function.

If the reflectivity function $f(\mathbf{n})$ is sampled from a sequence $\mathrm{F}_{\mathbf{n}}$ of *i.i.d.* copies of the random variable F, then, by the ergodic theorem, the empirical distribution of $f(\mathbf{n})$ converges to the theoretical distribution of F as N increases. Similarly, the estimate $y(\mathbf{n})$ of the reflectivity function $f(\mathbf{n})$ is, in fact, a filtered version of the white noise, and, thus, by the same ergodicity argument, its empirical distribution tends to the theoretical distribution of the corresponding random variable y as N tends to infinity. Due to the above associativity between the limiting empirical and the corresponding theoretical distributions, one can assert [35] that $y(\mathbf{n})$ is a good estimate of $f(\mathbf{n})$ to the same extent that y resembles F rather than a linear combination $\Sigma_{\mathbf{n}} z(\mathbf{n})\mathrm{F}_{\mathbf{n}}$. The latter, on the other hand, is always "more nearly" Gaussian than the individual components of the linear combination, i.e., F. In particular, using the calculus of variations under the normalization constraint $\|z\|_2 = 1$, one can show that [35]

$$\mathfrak{H}(\mathrm{Y}) = \mathfrak{H}\left(\sum_n z(\mathbf{n})\, \mathrm{F}_{\mathrm{n}}\right) \geq \mathfrak{H}(\mathrm{F}) \quad (14)$$

where $\mathfrak{H}$ denotes the *Shannon differential entropy*. Moreover, the equality in (14) is achieved if and only if either F is Gaussian or $z(\mathbf{n})=\delta(\mathbf{n}-\mathbf{n}_0)$, where $\delta(\mathbf{n})$ is the Kronecker delta function and $\mathbf{n}_0$ designates its arbitrary shift.

It is worthwhile noting that the entropy $\mathfrak{H}$ has long been known as an effective objective (or *contrast*) function, whose use in blind deconvolution dates back to the original idea of Wiggins [36] that seems to have triggered the development of the so-called *minimum entropy* deconvolution methods [35]. Moreover, the use of $\mathfrak{H}$ as a criterion in the inverse filter design may be shown to be consistent in the sense that, if the data sequence is obtained

as a convolution of an invertible filter with a white *non*-Gaussian noise, then the optimal inverse filter[1] will be a global minimizer of the entropy of the deconvolved result. This fact justifies using the ℓ_1-norm in (11), as it is straightforward to show that, under the Laplacian model, the empirical estimate of the entropy of a random variable is directly proportional to the ℓ_1-norm of the observations of the random variable. Thus, minimizations of $\mathfrak{H}(\mathrm{F})$ and $\|f\|_1$ are equivalent (at least from the numerical point of view).

The above considerations indicate that, in the case when the true reflectivity function is sparse, minimizing $E(\boldsymbol{\theta})$ given by (11) will result in convergence to the inverse filter that provides the sparsest reconstruction (as assessed by the ℓ_1-norm), whereas the latter, in turn, could be obtained only if the DFT-phase of the inverse filter was correctly identified (up to a linear slope). This is why we regard $E_2(\boldsymbol{\theta})$ given by (9) as a "facilitator" of convergence of the inverse filter to its optimal form.

V. Parametrization of the Inverse Filter

A. Regularization of Inverse Filtering

Since, in general, the PSF $h(\mathbf{n})$ tends to attenuate the out-of-band frequencies of the reflectivity function, the frequency response of the inverse filter is expected to grow significantly (and even to become unbounded) at higher frequencies. This fact immediately brings up issues of stability, which can result in inverse solutions of very limited use. In order for the reconstruction to be stable, the inverse filter should be *regularized*. It is well-known, however, that in the case when the reconstruction is performed via linear filtering, such a regularized filter, which is also optimal in the MSE-sense, is the deconvolution Wiener filter [37]. Furthermore, in the case when both $f(\mathbf{n})$ and $u(\mathbf{n})$ behave as mutually independent white noises, this Wiener filter can be defined in the Fourier domain by

$$W(\omega) = \frac{H^*(\omega)}{|H(\omega)|^2 + \epsilon} \quad (15)$$

where ε is a regularization parameter (called *inverse SNR*).

The effect of the regularization is exemplified in Fig. 1(A), which shows the real and imaginary parts of a 1-D PSF that has been obtained via demodulating an echo returned from a "point" target (a thin steel wire) in a water tank.[2] The measurements were performed using an unfocused, single-element, 3.5-MHz transducer (Panametrics V383, Waltham, MA) for both transmission and reception. Fig. 1(B) shows the amplitude of the DFT of the PSF that is seen to rapidly converge to zero at higher frequencies, thereby implying that the inverse problem is illposed. On the other hand, Fig. 1(C) and (D) shows the complex components of the Wiener filter and the amplitude of its DFT, respectively, where the Wiener filter was computed according to (15) with $\varepsilon = 10^{-4}$. One can see that the DFT of the Wiener filter converges to zero at higher frequencies. This property allows the filter to avoid amplifying those frequency components of the data which are dominated by noise. Consequently, to render the inverse filtering by $S(\boldsymbol{\omega})$ stable, it is imperative to force the shape of $S(\boldsymbol{\omega})$ to be as close as possible to that of $W(\boldsymbol{\omega})$.

[1]Here, by the optimal filter, we mean the filter that recovers the original signals up to a scalar multiplier and a shift.

[2]It should be noted that, strictly speaking, the reflectivity function of such a steel wire cannot be assumed to be a delta function, but rather a slightly smoothed version of the latter [38]. However, as the rate of convergence of this "smoothed delta" is still notably higher than that of the actual PSF, it is reasonable to assumed that the measured and actual PSF are close, and, therefore, their Fourier transforms should possess similar properties.

B. Standard Parametrization and Its Drawbacks

Certainly, the most common parametrization of $S(\boldsymbol{\omega}|\boldsymbol{\theta})$ is by the samples of its corresponding impulse response $s(\mathbf{n})$ [12], [24]. In this case, the inverse filter has the form of (4) with $\Psi_{\mathbf{k}}(\boldsymbol{\omega}) = \exp\{-i(\mathbf{k}\cdot\boldsymbol{\omega})\}$ and $\boldsymbol{\theta} = \{s(\mathbf{k})\}$, where $s(\mathrm{k}) \in \mathbb{C}$ and $\mathbf{k} \in \Gamma$, with Γ being a *finite* subset of $\mathbb{Z}^d$. Specifically

$$S(\omega|\theta) = \sum_{k\in\Gamma} s(\mathrm{k}) \exp\{-i(\mathrm{k}\cdot\omega)\}. \quad (16)$$

In the case when $s(\mathbf{n})$ is a causal FIR filter, the subset Γ can be defined as $\Gamma \equiv \Gamma(\mathbf{L}) = \{\mathbf{k}|0 \le k_j \le L_j - 1, \ \forall_j \in \{1,2, \ldots, d\}\}$, where $\mathbf{L} \equiv [L_1, L_2 \ldots, L_d]$ is a d-dimensional vector of positive integers which define the filter extent along corresponding dimensions.

Although being very natural and convenient to use, the parameterization (16) has a number of critical drawbacks in the case of band-limited PSF. This is because that the finiteness of the support of $s(\mathbf{n})$ implies that its DFT is given by a finite Fourier series that consists of the complex exponentials at relatively low frequencies. It is well-known, however, that due to the unboundedness of the support of the complex exponentials, a finite Fourier series cannot be endowed with an arbitrarily fast rate of convergence. Moreover, for nontrivial $s(\mathbf{n})$, finite Fourier series are necessarily nonzero almost everywhere in $\mathbb{T}^d$.

The above property of the finite Fourier series presents a problem for the design of inverse filters. Indeed, in the case when the PSF is band limited, the DFT of a regularized (linear) inverse filter is band limited, as well [see Fig. 1(D)]. Moreover, the latter also has a "steep" transition between its pass and stop bands. As a result, an accurate approximation of such a filter by the Fourier series (16) would require rather more than a few exponentials, and this is why, in most cases, regularized inverse filters have *infinite* impulse responses. This property of (16) inevitably leads to a "tradeoff" between the numerical stability and accuracy of the inverse filtering.

To overcome the above deficiency of the "standard" parameterization (16), we propose to replace the complex exponentials by functions $\{\Psi_{\mathbf{k}}(\boldsymbol{\omega})\}$ with *compact support*. Note that, due to the compactness of the support of $\{\Psi_{\mathbf{k}}(\boldsymbol{\omega})\}$, it is no longer a problem to obtain an $S(\boldsymbol{\omega})$ with an arbitrary "steep" stopband/passband transition and a virtually infinite attenuation within the stop-band using relatively small number of parameters $\boldsymbol{\theta}$. In this paper, the set $\{\Psi_{\mathbf{k}}(\boldsymbol{\omega})\}$is defined using the notion of *principle shift-invariant* (PSI) subspaces, which is briefly introduced next.

C. Compact Parametrization of Inverse Filters

The concept of PSI subspaces has been comprehensively studied in several works as a specific instance of shift-invariant subspaces [25], [26]. In the 1-D case, given an *admissible generator* $\varphi \in \mathbb{L}_2(\mathbb{R})$ of (typically) compact support, the corresponding PSI subspace $\mathscr{V}(\varphi)$ is defined as a subspace spanned by all the *integer* shifts of φ, i.e., $\mathscr{V}(\varphi) = \mathrm{span}\{\varphi(\cdot - k) \, k \in \mathbb{z}\}$. Note that the admissibility of φ requires it to be chosen in such a way that the set $\{\varphi_k = \varphi(\cdot - k)\}_{k\in\mathbb{Z}}$ is linearly independent and, hence, constitutes a Riesz basis in $\mathscr{V}(\varphi)$. This requirement is known to be fulfilled when the Fourier transform $\widehat{\varphi}$ of φ does not possess 2π-periodic zeros [26]. Moreover, if $\widehat{\varphi}$ has p-order zeros at each $\omega \in 2\pi\mathbb{Z}\setminus\{0\}$ (while being nonzero everywhere else), then $\mathscr{V}(\varphi)$ can be used to *stably* represent polynomials of degree $(p-1)$ on the intervals $[2^J k, 2^J(k+1)]$, where $k = 0, 1, \ldots, M-1$ [39].

Before defining a PSI subspace over $\mathbb{T}^d$, we first note that the subspace $\mathcal{V}(\varphi)$ defined above can be scaled using a *resolution* parameter $J \in \mathbb{Z}^-$. In particular, a "J-scaled" version $\mathcal{V}_J(\varphi)$ of $\mathcal{V}(\varphi)$ can be defined as $\mathcal{V}_J(\varphi) = \text{span}\left\{\varphi_{J,k}(\omega) = \sqrt{2^{-J}}\varphi\left(2^{-J}\omega - k\right) | k \in \mathbb{Z}\right\}$. Note that if φ is admissible, then the set $\{\varphi_{J,k}$ is also guaranteed to be a Riesz basis in $\mathcal{V}_J(\varphi)$. Moreover, the scaled subspace $\mathcal{V}_J(\varphi)$ can be periodized to obtain a subspace $\mathcal{V}_J^{2\pi}(\varphi)$ of functions defined over $\mathbb{T}$ given by

$$\mathrm{V}_J^{2\pi}(\varphi) = \text{Span}\left\{\varphi_{J,k}^{2\pi}\right\} \quad (17)$$

where $\varphi_{J,k}^{2\pi}(\omega) = \left(2^{J+1}\pi\right)^{-1}\Sigma_{l\in\mathbb{Z}}\varphi\left(2^{-J}(\omega/2\pi + l) - k\right)$, with $k = 0, 1, \ldots, 2^{-J} - 1$. It should be emphasized that the periodized PSI subspace $\mathcal{V}_J^{2\pi}(\varphi)$ is finite dimensional, since it has only 2^{-J} basis functions.

The subspace $\mathcal{V}_J^{2\pi}(\varphi)$ can be thought of as an *approximation* subspace for the functions in $\mathbb{L}_2(\mathbb{T})$. The properties of $\mathcal{V}_J^{2\pi}(\varphi)$ as an approximant are intimately related to those of the generator φ[25]. For the case at hand, we note that for an arbitrary $u \in \mathbb{L}_2(\mathbb{T})$, the error of its approximation in $\mathcal{V}_J^{2\pi}(\varphi)$ can be shown to behave like $\|u - \mathcal{P}_\mathcal{V}\{u\}\|_{\mathbb{L}_2} = \mathcal{O}\left(2^{J\quad p}\right)$, where $\mathcal{P}_\mathcal{V}$ denotes the operator of orthogonal projection onto $\mathcal{V}_J^{2\pi}(\varphi)$ and p is a scalar related to the degree of regularity of the generator $\varphi(\omega)$.[3] From this perspective, the parameter J can be thought of as a resolution parameter in the sense that the smaller J parameter is, the narrower the support of $\varphi_{J,k}^{2\pi}$ and, therefore, the higher the approximation order of the subspace $\mathcal{V}_J^{2\pi}(\varphi)$.

The construction of the subspace $\mathcal{V}_J^{2\pi}(\varphi)$ can be easily extended in higher dimensions by means of the separable tensor product. In particular, a PSI subspace over $\mathbb{T}^d$ can be defined as

$$\mathcal{V}_\mathbf{J}^{\mathbb{T}^d} = \text{Span}\left\{\Phi_{J,k}\right\} \quad (18)$$

where

$$\Phi_{J,k}(\omega) = \prod_{j=1}^{d}\varphi_{k_j,J_j}^{2\pi}\left(\omega_j\right) \quad (19)$$

with $\mathbf{J}$ being a d-dimensional vector of negative integers $[J_1, J_2, \ldots, J_d]^T$, which control the resolution of $\mathcal{V}_J^{\mathbb{T}^d}$ along the corresponding dimensions. Quite intuitively, if the generator φ is admissible, then the set $\{\Phi_{\mathbf{J},\mathbf{k}}\}$ is necessary linearly independent, and, hence, the PSI subspace (18) can be used for stably approximating 2π-periodic functions from $\mathbb{L}_2\left(\mathbb{T}^d\right)$.

Having defined the periodic PSI subspace $\mathcal{V}_J^{\mathbb{T}^d}$ via (18), we propose to model the real and imaginary parts of the DFT $S(\omega|\theta)$ of the inverse filter $s(\mathbf{n})$ as members of this subspace, with the latter being generated for some φ and a predefined value of $\mathbf{J}$. In order to formalize this construction, we first let the index set $\Upsilon(\mathbf{J})$ be defined as $\Upsilon(J) = \{k | 0 \le k_j \le 2^{-J_j} - 1, \forall j \in \{1,2,\ldots,d\}\}$. Then, the proposed parameterization conforms to (4) by setting $\Psi_\mathbf{k}(\omega) =$

[3] In this paper, we used a compactly supported cubic B-spine as a generator for the corresponding PSI subspace. In this case, $p = 4$.

$\Phi_{\mathbf{J},\mathbf{k}}(\boldsymbol{\omega})$, where $\Psi_{\mathbf{k}}(\boldsymbol{\omega})$ is understood to be a complex-valued function from $\mathbb{T}^d$ to $\mathbb{C}$, with its real and imaginary parts being equal to $\Phi_{\mathbf{J},\mathbf{k}}(\boldsymbol{\omega})$ and zero, respectively. Formally

$$S(\omega|\theta) = \sum_{\mathrm{k}\in\Upsilon(\mathrm{J})} \theta_{\mathrm{k}} \Phi_{J,k}(\omega) \quad (20)$$

with $\theta_k \in \mathbb{C}, \forall \mathrm{k} \in \Upsilon(\mathbf{J})$. For the sake of convenience, from now on, the parametrization (20) will be referred to as "compact" (alluding to the compactness of the support of the basis functions).

Finally, before turning to a discussion on some numerical aspects for the minimization of the functionals given by either (11) or (12), the validity of the "compact" parameterization (20) needs to be established. In addressing this important question, we note that, under the assumption that $s(\mathbf{n})$ is absolutely summable, its DFT $S(\boldsymbol{\omega})$ is necessarily a uniformly continuous function. Therefore, there always exists $\mathbf{J}$ and the corresponding unique parameters $\{\boldsymbol{\tau}_{\mathrm{k}}\}_{\mathrm{k}\in\Upsilon(\mathbf{J})}$ such that the norm of the difference between $S(\boldsymbol{\omega})$ and its orthogonal projection onto $\mathscr{V}_{\mathbf{J}}^{\mathbb{T}^d}$ will be less than any predefined $\varepsilon > 0$ [25]. However, a rigorous way to define the resolution of a PSI subspace that would be necessary to achieve a required approximation accuracy requires formally specifying the functional space to which the PSF belongs. This would allow us to define the smoothness properties of the DFT of the PSF, and subsequently those of its (regularized) inversion. As a final point, the desired $\mathbf{J}$ could be inferred using the basic results of the theory of PSI subspaces. However, such a rigorous analysis is omitted in this paper, since it would have taken us too far astray from our main goal—the proposal of a practical algorithm for the deconvolution of ultrasound images. Based upon our belief that the above analysis certainly deserves a separate and more ample treatment, in the present paper, the viability of the proposed parameterization is proven indirectly via comparing the results of our experimental study given below.

VI. Numerical Implementation of Inverse Filtering

A. Regularization Revised

As noticed in Section IV-A, the Lebesgue measure $d\mu(\boldsymbol{\omega})$ in (7) is intended to render the problem of minimizing the functional $E_1(\boldsymbol{\theta})$ well-posed in the case of band-limited PSF. When the functions under consideration are continuous, this measure can be defined by means of a *density* function $\rho(\boldsymbol{\omega})$, so that $d\mu(\boldsymbol{\omega}) = \rho(\boldsymbol{\omega})$. During the experimental phase of this study, however, it was observed that the density $\rho(\boldsymbol{\omega})$ can be set to be equal to unity over the whole domain of integration $\mathbb{T}^d$, if the cost functional in (11) is complemented by a simple ("Tikhonov-type" [40]) regularization term $\|\theta\|_2^2$ which is supposed to penalize the ℓ_1-energy of the parameters of the inverse filter. In this case, the cost functional (11) becomes

$$E_{\mathrm{HBD}}(\theta) = \int_{\mathbb{T}^d} \eta\left(|S(\omega|\theta)\,|\widehat{H}(\omega)|^2 - 1\right) d\omega + \lambda \|\mathscr{F}^{-1}\{S(\omega|\theta)\,G(\omega)\}\|_1 + \mu\|\theta\|_2^2. \quad (21)$$

where $\mu > 0$ is a design constant, and the subscript "HBD" is introduced to concretize that the functional (21) corresponds to the "hybrid" design of the inverse filter.

It should be noted that, even though the functionals (11) and (21) were observed to result in virtually identical solutions for the inverse filter, the latter was found preferable from the perspective of its numerical minimization. This is because of the property of $\mu\|\theta\|_2^2$ being a convex function of $\boldsymbol{\theta}$, which contributes to the overall convexity of $E_{\mathrm{HBD}}(\boldsymbol{\theta})$. A practical implication of this fact is that Newtonian-type optimization methods are able to converge to

the minima of $E_{\mathrm{HBD}}(\boldsymbol{\theta})$ in considerably faster rates as compared with their convergence to the minima of $E(\boldsymbol{\theta})$ given by (11).

By analogy, the same convex term $\|\theta\|_2^2$ can be added to the ML cost functional (12) resulting in

$$E_{\mathrm{ML}}(\theta) = -\int_{\mathbb{T}^d} \log|S(\omega|\theta)|\,d\omega + \lambda\|\mathscr{F}^{-1}\{S(\omega|\theta)\,G(\omega)\}\|_1 + \mu\|\theta\|_2^2. \quad (22)$$

However, while in the case of (21), the addition of $\mu\|\theta\|_2^2$ was done in order to improve the numerical characteristics of the resulting minimization, in the case of (22) this becomes a necessity. The fact is that, for the PSF used in the present study, without adding this term, it was found impossible to achieve stable convergence to the local minima of (12) for *any* value of parameter λ. This issue of stability of the ML design of the inverse filter was recently addressed in [41], where it was shown that the cost functional (22) can be formally obtained via reformulating the problem of estimation of the inverse filter within the framework of MAP estimation.

It goes without saying that properly determining the regularization parameters is crucial for the inverse filtering results to be stable and reliable. In particular, the values of the regularization parameters λ and μ in (21) and (22) are mainly dependent on the degree of ill-posedness of the operator of convolution with the PSF as well as on the level of additive noises. Moreover, since the ill-posedness of the convolution is defined by the aperture geometry, central frequency, and bandwidth of an ultrasound transducer in use, one should expect to observe different optimal values of the parameters for different transducers. However, while evident in processing of RF-data, the above dependency appears to be much less noticeable when IQ-signals were dealt with. This is because, after having been subjected to the processes of demodulation and downsampling, the spectra of IQ-signals appear to be similarly shaped, with their central frequencies being around zero and their bandwidths fitting the entire band $\mathbb{T}^d$. This seems to be the main reason for the observation that as long as IQ-images are processed, the optimal values of parameters λ and μ change insignificantly when different types of PSF and tissues are used. On the other hand, the dependency of the optimal values of the regularization parameters on the noise levels should not be neglected. In particular, it was observed that the optimal values of μ change proportionally to the variance of the additive noise $u(n)$, with $\mu \in [0.01, 0.05]$ for SNR = 14 dB. Hence, μ seems to function in a similar manner as the inverse-SNR in Wiener filtering. At the same time, the dependency of parameter λ on the noise variance was found to be much less pronounced. In particular, it was observed experimentally that, for SNR ranging between 7 and 20 dB, the values of λ in the interval [0.1, 0.5] worked satisfactory for all tissues and PSFs tested in this study (with larger λ corresponding to noisier data). Note that, in this study, the particular values of μ and λ have been chosen by trial and error within the above intervals so as to maximize the quality of resulting estimates.

B. Numerical Optimization Method

In this work, all cost functionals were minimized using the Newton method, which is known to be among the most efficient tools of unconstrained optimization [42]. The standard Newton minimization of functional $E(\boldsymbol{\theta})$ consists in iteratively finding its minimizer according to

$$\theta^{t+1} = \theta^t + \alpha_t \mathbf{d}^t \quad (23)$$

where α_t is determined via the *line search* $\alpha_t = \arg\min_\alpha E(\boldsymbol{\theta}^t + \alpha\mathbf{d}^t)$ with $\mathbf{d}^t$ being the *Newton direction*, which is computed as a solution to the following system of equations:

$$\nabla^2 E\left(\theta^t\right) \mathrm{d}^t = -\nabla E\left(\theta^t\right). \quad (24)$$

Here, $\nabla E(\boldsymbol{\theta}^t)$ and $\nabla^2 E(\boldsymbol{\theta}^t)$ denote the gradient and the Hessian of the functional $E(\boldsymbol{\theta})$, respectively, evaluated at the iteration point $\boldsymbol{\theta}^t$.

It is worthwhile noting that, independently of the given parameterization, the parameters $\boldsymbol{\theta}$ of the inverse filter $S(\boldsymbol{\omega}\ \boldsymbol{\theta})$ can be arranged (via the lexicographic ordering, for example) as a complex vector of dimension N, with the latter equal to the cardinality of either the set $\Gamma(\mathbf{L})$ in (16) or the set $\Upsilon(\mathbf{J})$ in (20) (depending on whether the parametrization is standard or compact). In this case, the functionals (21) and (22) can be considered to be *real-valued* functions of a complex vector, whose first and second derivatives can be computed by the standard methods of calculus.

Due to the use of second-order information on the minimization functional $E(\boldsymbol{\theta})$ (i.e., its Hessian), the Newton algorithm often provides a quadratic rate of convergence near the optimal point. However, as $E(\boldsymbol{\theta})$ is nonconvex for the case at hand, the direction $\mathbf{d}^t$ as defined by (24) cannot be guaranteed to be a descent direction for all t. To alleviate this problem, we solve the system (24) using the *modified Cholesky factorization* algorithm [42], which replaces $\nabla^2 E(\boldsymbol{\theta}^t)$ by $\nabla^2 E(\boldsymbol{\theta}^t) + \Delta$, where Δ is a diagonal matrix. The latter is chosen automatically to guarantee that $\nabla^2 E(\boldsymbol{\theta}^t) + \Delta$ is positive definite, and, as a result, $\mathbf{d}^t = (\nabla^2 E(\boldsymbol{\theta}^t) + \Delta)^{-1} \nabla E(\boldsymbol{\theta}^t)$ defines a descent direction.

C. Optimization Complexity

In order to digitally implement the inverse filtering, the functional (21) [or, alternatively, (22)] needs to be discretized. The discretization amounts to replacing the Fourier transforms by their sampled versions and approximating the integrations by finite summations. Thus, in practice, all the computations are supposed to be performed over a *discrete* subset Ω_M of $\mathbb{T}^d$, which is usually obtained through uniformly sampling the latter at M discrete points. In the current study, M was set to be equal to the number of samples of IQ-data (implying that no oversampling was used).

The speed of minimization of both E_{HBD} and E_{ML} is largely determined by the complexity of evaluating (16) and (20), respectively, as well as by the complexity of computing the inner product between an arbitrary function from $\mathbb{L}_2\left(\mathbb{T}^d\right)$ and the functions of the set $\{\Psi_{\mathbf{k}}(\boldsymbol{\omega})\}$. In the case of the standard parametrization, these operations requires only a few FFT operations, which can be performed with logarithmic complexity $\mathcal{O}(M \log M)$. In the case of the compact parametrization, the same operations may be performed by convolutions with FIR filters as detailed in [43], [44], and, thus, their complexity is basically linear, i.e., $\mathcal{O}(M)$. However, as computing the second term in either (21) or (22) still requires FFT operations, the overall complexity of the computations here remains logarithmic, as well.

Finally, we note that the ℓ_1-norm involved in the definition of the cost functionals is not a smooth function, and, hence, it should be replaced by its smooth approximation to make the Newton optimization technique well defined. For such an approximation, we use $\|z\|_1 \simeq \Sigma_k \sqrt{\Re(z_k) + \Im(z_k) + \epsilon}$, where $\Re$ and $\Im$ stand for the real and imaginary parts, respectively, and $0 \leq \varepsilon$ [ckr] 1.[4]

[4]In our computations, we used $\varepsilon = 10^{-3}$.

VII. MAP Formulation of Blind Deconvolution Problem

A. Nonblind Deconvolution Versus Inverse Filtering

In the case of the "hybrid" approach, the estimated inverse filter can be further used for estimation of the PSF according to (6). The estimated PSF, in turn, can be used to perform nonblind deconvolution of IQ-images, which has a number of advantages over the linear filtering. In particular, nonblind deconvolution can be advantageous, since it admits a closed form solution via Wiener filtering (15), thereby allowing the possibility of a fast implementation. Additionally, in the case of nonblind deconvolution, it is easy to incorporate diverse statistical priors on the tissue reflectivity function. As a result, once the PSF is known, it is no longer crucial to stick to the assumption of "sparse tissue," which plays the central role in the proposed method for estimating the inverse filter (see Section IV-C). Finally, the inverse filtering is a linear operator, and, hence, it is incapable of interpolating the spectral components of the tissue reflectivity function which are lost in the process of image formation. On the other hand, among nonblind deconvolution methods, a number of nonlinear algorithms are available which can successively interpolate the lost spectral components. For the above reasons, the nonblind deconvolution should be considered as an important boosting stage supplementing the inverse filtering.

B. MAP Estimation of the Reflectivity Function

It is well known that for smooth PSF, the solution of the deconvolution problem does not depend continuously on the data, and hence, the problem of recovering the reflectivity function is ill-posed. However, this solution can be rendered stable via incorporating some *a priori* information on the function to be recovered. This can be conveniently done using a statistical estimation framework, within which the MAP estimation provides the most likely solution given the observed data and a reasonable assumption regarding the statistical nature of the object of interest [27]. Specifically, in the case when the measurement noise and the tissue reflectivity function can be assumed to be mutually independent white Gaussian noise, the MAP estimate of the reflectivity function can be shown to be given by the Wiener filtering (15) [45]. The main shortcoming of this method, however, is the Gibbs-like artifacts, which are usually produced by the filter near discontinuities of $f(\mathbf{n})$. Moreover, being linear in nature, the Wiener filter is incapable of interpolating the information lost in the process of image formation. As a result, the Wiener solutions are frequently overly smoothed.

In the case when the samples of the reflectivity function are assumed to be independent, zero-mean random variables obeying the Laplacian distribution (corresponding to the assumption of "sparse tissue"), the MAP estimation requires solving the minimization problem given by [7] and [33]

$$\min_f \left\{ \|f * h - g\|_2^2 + \gamma \|f\|_1 \right\} \quad (25)$$

where $\gamma > 0$ is a regularization parameter.

The minimization problem (25) results from assuming $f(\mathbf{n})$ to be "sparse." Note that the very same assumption underpinned the design of the inverse filtering in Section IV-B. However, it should be noted that assuming the same statistical properties for the reflectivity function does *not* produce identical results in both cases. This is because the highly nonlinear nature of the MAP estimation (25) allows it to interpolate the high-frequency harmonic components of the reflectivity function, which have been destroyed by convolution with a band-limited PSF. On the other hand, being linear in nature, the inverse filtering cannot achieve an analogous result.

Finally, we note that, in this paper, the minimization of (25) was performed using the *truncated* Newton method [46], with the regularization parameter γ set empirically so as to obtain the most reasonable results.[5] We also note that (25) can be reformulated as the problems of minimizing the norm $\|f\|_1$ subject to $\|f * h - g\|_2^2 \leq k$, where κ is an "SNR-dependent" constant. This problem could be efficiently solved by means of Conic Programming [47].

VIII. Experimental Results

A. In Silico Experiments

In silico experimental study is commonly accepted as an important stage in the development of novel reconstruction methods, since it allows evaluating their performance under controlled conditions. In this paper, the simulation study has been conducted using 1-D RF-data. Note that the simulations have been confined to the 1-D case for the reason of its being more demonstrable and quickly computable, while being completely equivalent (from the viewpoint of the evaluation criteria used) to higher dimensional cases. The 1-D RF-sequences were simulated according to the model of (1) using the same PSF, whose complex counterpart is shown in Fig. 1(A). The reflectivity functions were simulated as random sequences of *i.i.d.* random variables obeying the zero-mean, *Generalized Gaussian* (GG) distribution, whose *pdf* is defined as

$$p(x) = \frac{\nu}{2\sigma}\frac{\eta(\nu)}{\Gamma(\nu^{-1})}\exp\left\{-\left(\frac{\eta(\nu)|x|}{\sigma}\right)^{\nu}\right\} \quad (26)$$

where σ is the standard deviation, ν is the shape parameter, $\eta(\nu) = \sqrt{\Gamma(3\nu^{-1})\Gamma^{-1}(\nu^{-1})}$, and Γ is the Gamma function. Note that the GG distribution contains the Laplacian distribution as a special case, when $\nu = 1$. In the course of the simulations, a number of values for ν in the range [0.6, 1.4] were tried to investigate the robustness of the deconvolution to violation of the assumption of "Laplacian tissue." However, since the resulting estimates showed robustness to the value of ν, throughout the rest of the simulation study, ν was set to be 1.

The length of all simulated RF-sequences was set to be equal to 512 sample points, which would have corresponded to the interrogation depth of approximately 40 mm, if the sequences were acquired *in vivo* at the sampling rate of 20 MHz. All the RF-sequences were corrupted by white Gaussian noise of different sizes that gave rise to a number of values of SNR, namely, 10, 14, and 20 dB. Subsequently, the simulated RF-sequences were filtered, demodulated, and subsampled by the factor of 4 resulting in a set of related IQ-sequences. Fig. 2(A)-(C) demonstrates a simulated reflectivity function, the corresponding RF-sequence and the absolute value of the related IQ-sequence (commonly referred to as the *envelope*), respectively. Note that the envelope is shown against the absolute value of the reflectivity function.

The simulated IQ-sequences were used for estimation of the Fourier magnitude of the PSF according to the procedure discussed in Section III. The robust wavelet de-noising was based on the classical three-step algorithm of [48], which was implemented by means of the WaveLab package available at http://www-stat.stanford.edu/wavelab/. The universal threshold $\sqrt{2\log(M)}\tilde{\sigma}$ was used to perform soft-thresholding of wavelet coefficients. In the above formula, M was defined to be the length of the IQ-sequences, while $\tilde{\sigma}$ was set to

[5]Note that, in order for (25) to be solvable by means of a gradient-based optimization algorithm, the ℓ_1-norm $\|f\|_1$ should be approximated by a smooth function, e.g., as discussed in Section VI-C.

be equal to 0.5 that is the theoretically predicted standard deviation of the noise to be rejected.[6] The nearly symmetric wavelets of I. Daubechies with four vanishing moments [49, Ch. 6] were used to perform the wavelet decomposition.

Finally, the IQ-sequences were processed by different deconvolution algorithms, whose performances were being compared. All the inverse filters under comparison were parameterized using the same number of filter parameters. In particular, in the case of the standard parameterization, $S(\omega|\theta)$ was modeled as a linear combination of $M = 32$ complex exponentials, while in the case of the compact parameterization, a set of $M = 32$ B-splines (that corresponds to $J = -5$) was used to model the real and imaginary parts of $S(\omega|\theta)$ according to (20). Moreover, to make it possible to compare the deconvolution algorithms by their computational efficiency, the functionals (21) and (22), as well as their derivatives, were computed by means of explicit vector-matrix multiplications.

To assess the reconstruction quality, the deconvolved IQ-sequences were compared against the corresponding reflectivity functions. In order for such a comparison to be possible, the latter were demodulated and low-pass filtered using the filter $P(\omega)$ defined by

$$P(\omega) = \frac{|H(\omega)|^2}{|H(\omega)|^2 + \epsilon} \quad (27)$$

where ε is the inverse SNR. Note that applying the Wiener filter (15) to both sides of the model (2) results in $G(\omega)W(\omega) = P(\omega)F(\omega) + W(\omega)U(\omega)$. Consequently, assuming the noise $u(\mathbf{n})$ to be a zero-mean, white noise (while treating $F(\omega)$ as a deterministic quantity) implies that a demodulated reflectivity function obtained in the manner specified above is equal to the expected value of its estimate computed using the Wiener filter (15) with the *known* $H(\omega)$. Thus, since the Wiener filter is the optimal linear estimator, using the demodulated reflectivity functions filtered by (27) seems to be a reasonable reference.

In the following subsections, we will quantitatively compare all the tested deconvolution methods. As a quality measure, we will use the *normalized mean squared error* (NMSE) criterion defined as

$$\mathrm{NMSE}(\tilde{y}) = \varepsilon\left\{\frac{\|\tilde{y} - y\|_2^2}{\|y\|_2^2}\right\} \quad (28)$$

where y and $\tilde{y}$ denote the desired quantity and its estimate, respectively. In this paper, the expectation in (28) has been estimated based on the results of 200 independent trials.

1) Experiment 1: The objective of this experiment was to compare the proposed "hybrid" deconvolution approach with the formal ML approach, which are based on minimizing the functionals given by (21) and (22), respectively. The "hybrid" deconvolution method based on the "standard" (i.e., Fourier) and "compact" parameterization schemes will be referred below to as "Hybrid-Fourier" and "Hybrid-Spline" methods, respectively. By analogy, the corresponding ML methods will be referred to as "ML-Fourier" and "ML-Spline" methods. As an additional reference, the deconvolution results computed using the Wiener filter (15) for the *known* PSF are provided as well. The latter method will be referred to as "Oracle Wiener" (metaphorically implying that such estimation could only be possible, if an oracle provided us with the true PSF).

[6]Note that, in the current case, by the noise, we mean the log magnitudes of the DFT of reflectivity functions, after they have been subjected to the procedure of outlier shrinkage, as detailed in [17].

Table I summarizes the NMSE computed for the original IQ-envelope and for different reconstruction methods. Analyzing this table, one can see that the "Oracle Wiener" provides the best result reducing the NMSE of the original envelope by an average factor of 8.96. However, among the blind deconvolution methods, the best performer is "Hybrid-Spline," which reduces the NMSE of the original envelope by an average factor of 7.05. At the same time, analogous factors for the "Hybrid-Fourier," "ML-Spline," and "ML-Fourier" methods were found to be 2.39, 1.39, and 1.09, respectively. Therefore, one can conclude that the "hybrid" methods perform considerably better than the ML methods. Furthermore, between the two "hybrid" algorithms, "Hybrid-Spline" results in the NMSE, which is three times smaller than the error of "Hybrid-Fourier."

Fig. 3 shows an example of the estimation results obtained by (top-to-bottom) "Hybrid-Spline," "Hybrid-Fourier," "ML-Spline," and "ML-Fourier" (solid lines) versus the corresponding demodulated reflectivity function (dotted line). One can see that "Hybrid-Spline" obviously provides the most accurate reconstruction. Additionally, the left column of Fig. 4 shows the DFT magnitudes of the inverse filters corresponding to (top-to-bottom) the "Hybrid-Spline," "Hybrid-Fourier," "ML-Spline," and "ML-Fourier" methods, while the right column shows the related combined frequency responses. One can see that the DFT magnitude of the inverse filter of "Hybrid-Spline" has the form of the optimal Wiener filter [see Fig. 1(D) for comparison]. Moreover, the amplitude of the combined response of "Hybrid-Spline" has the desired properties of a band-limiting filter. The inverse filter of "Hybrid-Fourier" also has its spectral shape resembling that of the Wiener filter. However, in this case, the presence of the Gibbs phenomenon implies nonzero amplification out of the passband. Moreover, the combined response of "Hybrid-Fourier" also exhibits the "ringing" effect that stems from the property of complex exponentials to be noncompactly supported functions. Finally, we note that the spectral shapes of the inverse filters corresponding to "ML-Spline" and "ML-Fourier" are of high-pass type. However, due to the lack of regularization, their spectral shapes, as well as those of their combined responses, are intractable.

In addition to NMSE, the deconvolution methods were compared using some other performance measures. As it was pointed out in Section II, the inverse filtering can perform the estimation only up to an arbitrary "shift" error, which can be used to compare the algorithms. Additionally, the average number of Newton iterations which are required to reduce the norm of the gradient of the cost functions below 10^{-6}, together with the average duration of one Newton iteration, also constitute informative measures that can used for comparison.

The mean values of the above measures (as computed based on the results of 200 independent trials) are tabulated in Table II. One can see that the methods using the compact parameterization have zero "shift" error and faster convergence, as compared to the methods based on the standard parametrization. In particular, comparing "Hybrid-Spline" with "ML-Fourier," one can see that, on average, the former requires about 4.3 times fewer iterations than the latter does. Moreover, the duration of one Newton iteration for "Hybrid-Spline" is about 1.5 times shorter than that for the "ML-Fourier" method.

2) Experiment 2: The experiments of Section VIII-A1 have demonstrated that the "Hybrid-Spline" deconvolution method significantly outperforms the alternative approaches. In this section, we compare the results of *non*-blind deconvolution of IQ-sequences. To this end, we estimate the PSF according to (6) with $S(\omega)$ being the inverse filter computed by the "Hybrid-Spline" method, and compare the performance of the Wiener filtering (15) with that of the nonlinear MAP estimation (25). Below, these methods are referred to as "Blind Wiener" and "Blind Sparse," respectively.

Fig. 5(A)-(D) shows the estimates (solid lines) of a reflectivity function (dotted line) computed by means of the "Oracle Wiener," "Hybrid Spline," "Blind Wiener," and "Blind Sparse" algorithms, respectively. One can see that, while all the linear solutions are of comparable quality, the solution computed by the "Blind Sparse" method has superior resolution, thereby much better representing the reflectivity function. Unfortunately, we have found it very difficult to compare the above results quantitatively, as the NMSE criterion turned out to be no longer suitable for this purpose. This is because the nonlinear solution by the "Blind Sparse" method does not belong to the same "signal subspace" as the linear solutions. This fact is illustrated in Fig. 6 which shows the DFT magnitudes of the estimates depicted in Fig. 5. One can see that, while in the case of linear estimation, all the resulting DFT are supported over the transducer passband, the spectrum of the estimate computed by the "Blind Sparse" method is virtually white.

In order to compare the above methods in a quantitative way, a different criterion was used. In particular, the width of the autocorrelation function of the envelope of a deconvolved IQ-sequence, as measured at its -3-dB level, was used to assess the resolution improvement [6]. Fig. 7 shows the autocorrelation function of an original IQ-sequence (dotted line) together with those of its deconvolved versions (solid lines) computed using (top-to-bottom) the "Oracle Wiener," "Hybrid-Spline," "Blind Wiener," and "Blind Sparse" methods, respectively. One can see that the autocorrelation function corresponding to the nonlinear "Blind Sparse" method has a much faster rate of convergence than those of the linear methods, thereby implying a higher resolution gain. Specifically, the resolution improvement by the "Blind Sparse" method was found to be 7.29, while for the "Oracle Wiener," "Hybrid-Spline," and "Blind Wiener" methods it was equal to 1.64, 1.58, and 1.64, correspondingly.

B. In Vivo Experiments

As a next step, the proposed deconvolution algorithms were compared using *in vivo* ultrasound data. To this end, a set of RF-images was recorded from adult volunteers with a VIVID3 (GE Medical Ultrasound, Inc.) commercial ultrasound scanner equipped with a special (digital) data-transfer board. The recorded set of images was comprised of 15 abdominal and 15 vascular images, acquired using C358 and 546L probes, respectively.[7] All the images were acquired with a single transmission focal point, localized approximately at the center of the field of view. The sampling rate and resolution of data acquisition were 20 MHz and 14 bits, correspondingly.

Each of the acquired RF-images was partitioned into several overlapped image segments along the radial direction. The length of the segments was set to be 512 sample points. Subsequently, the resulting segments were demodulated, subsampled by a factor of 4, and deconvolved. As a final step, the nonoverlapped portions of the deconvolved image segments were "stacked up" to produce the whole-image reconstructions, whose absolute values were normalized and log compressed for visualization in 8-bit resolution (so that all the images presented in this paper have the same dynamic range). The fast scan conversion method of [50] was used to transform the abdominal images to the polar coordinate system.

In the *in vivo* study, we compared the performance of the "Hybrid-Spline" and "Blind-Sparse" algorithms with that of the homomorphic deconvolution method of [6], which will be referred to below as the "cepstrum-based" deconvolution. It should be noted that the switch-over to a different reference method has been a necessary step, since for the data at hand, no parameters of the ML design (22) of the inverse filter could be found for which the

[7]A detailed specification of the probes is available at the manufacturer's website at http://www.gehealthcare.com/helpcenter/html.

latter would provide stable reconstruction. On the other hand, the process of "cepstrum-based" deconvolution consists of two stages: the PSF is first estimated using the homomorphic relationship (5) [14], followed by *non*-blindly deconvolving the related image. Since the latter stage can always be regularized (e.g., using the MAP estimation framework of Section VII-B), it is normally not a problem to implement the "cepstrum-based" deconvolution in a stable manner. In the current paper, the nonblind deconvolution is performed using the Wiener filter (15), as it was proposed in [6].

In the *in vivo* experiments, the resolution parameter **J** of the "Hybrid-Spline" method was set to be equal to [4, 4], while in the case of the "cepstrum-based" deconvolution, the cepstral cutoff parameters were set empirically so as to produce the most accurate reconstruction results in terms of the minimality of blurring artifacts and the maximality of image contrast.

The obtained deconvolution results were similar for all the acquired images. A typical result is shown in Fig. 8(A): an original (i.e., unprocessed) fragment of the image of a right kidney. At the same time, Fig. 8(B) and (C) shows the deconvolved images computed by the "cepstrum-based" and "Hybrid-Spline" algorithms, respectively, while Fig. 8(D) shows the reconstruction obtained by means of the "Blind-Sparse" deconvolution. Clearly, the latter provides the result of superior quality as judged by the apparent gain in both image resolution and contrast. One can see that all structures within the "Blind-Sparse" reconstruction appear considerably less blurred than in the original image. At the same time, the property of the "cepstrum-based" and "Hybrid-Spline" methods of being linear estimators does not allow them to achieve analogous results. Although these methods produce deconvolved images the speckle patterns of which are noticeably "finer" than that of the original image, the linearly reconstructed images still appear to be lacking in high-frequency components. It should be noted, however, that the reconstruction obtained by the "Hybrid-Spline" method seems to be somewhat "sharper" as compared with the reconstruction obtained by the "cepstrum-based" deconvolution. This might be caused by sizable inaccuracies in estimating the PSF by the latter approach. Such a conclusion, however, is hard to vindicate based on merely visual observations of the deconvolution results because of both an intricate nature of the represented anatomy and the unavailability of the "true" reflectivity function.

To support the above conclusion a different *in vivo* result is demonstrated in Fig. 9(A): an original fragment of the longitudinal view of a carotid artery. The image has been chosen over the others owing to its explicit anatomical structure that includes a portion of the vessel's intima appearing as two oblong "stripes" near the upper and lower boundaries of the lumen. Because of the relatively low resolution of the ultrasound scanner, however, the intima can be seen to be poorly separated from the neighboring tissue in the image plane. Thus, deconvolution is expected to result in a reconstructed image in which the intima is represented in a more clear-cut manner. Unfortunately, the "cepstrum-based" deconvolution, whose result is shown in Fig. 9(B), does not seem to be capable of producing such a reconstruction. Even though the speckle pattern of the deconvolved image is seemingly finer than that of the original image, one can see that the intima (as well as the overall wall-lumen interface of the artery) have remained considerably blurred—the effect that is likely to have been caused by inaccuracies in estimating the PSF. On the other hand, Fig. 9(C) shows the reconstruction obtained by means of the "Hybrid-Spline" method. One can see that, in this case, the deconvolved image provides a far clearer representation of vessel's anatomy as compared to the previous results. Moreover, due to the increase in image resolution, those portions of the intima which had been indistinguishable from the vessel wall, are now clearly separated (notice, in particular, the "upper" layer of the intima). This result can be further improved by using the "Blind-Sparse" method, as it is shown in Fig. 9(D). The

property of “Blind-Sparse” of being a nonlinear estimation method allows it to efficiently interpolate those spectral components of the reflectivity function which have been lost in the process of image formation. As a result, this method is capable of recovering the reflectivity structure of interrogated organs at a resolution substantially exceeding that of the linear estimators.

To qualify and compare the resolution gains provided by the (linear) “Hybrid-Spline” and (nonlinear) “Blind-Sparse” methods, the normalized 2-D autocorrelation functions of the standard and corresponding deconvolved images were computed (prior to performing the dynamic range compression and scan conversion). These functions are depicted in Fig. 10 where (A)–(C) correspond to the original image, the “Hybrid-Spline” solution, and the “Blind-Sparse” solution, respectively. A numerical measure of the resolution gain was defined by the ratio between the number of pixels of the autocorrelation function with values higher than 0.75, computed for the standard envelope image, and that for the deconvolved image [6]. The mean resolution gains obtained for the “Hybrid-Spline” method was 2.24, while the gain of the “Blind-Sparse” method was found to be 6.52.

IX. Discussion and Conclusions

This paper addresses the problem of blind deconvolution of medical ultrasound images by formulating a solution which is innovative in two main ways. First, the proposed methodology is based on recovering the tissue reflectivity function by means of linear inverse filtering, the design of which involves some partial information about the PSF. For the application at hand, this partial information is given by the power spectrum of the PSF, which is estimated directly from the IQ-data before the estimation of inverse filter is initiated. However, even though, in this paper, the deconvolution is structured as a two-stage process, in general, it does not need to be necessarily so. Indeed, we believe that the proposed technique can be applied for enhancing the resolution of optical images, in which case there is no need for estimating the power spectrum of the PSF, since it can be computed analytically based on the aperture geometry [51]. It should be noted that, from this perspective, the methodology described in this paper is conceptually different from approaches in which an initial estimate of the PSF is computed first, followed by its update via an optimization procedure [52].

The second contribution of this paper consists in the introduction of a different method for modeling the inverse transfer function. In particular, it was proposed to model the latter as a linear combination of compactly-supported basis functions, as opposed to the case of standard parameterization that is based on complex exponentials of infinite support. Such a “compact” parameterization was shown to result in considerably smaller reconstruction errors as compared to the standard case. The compactly-supported functions used for parameterizing the inverse filter were defined to be shifts of a scaled version of an admissible generating function (e.g., a cubic B-spline). In this case, the scale **J** is independent of the shift index, which makes the resulting approximations be nonadaptive to local variations of the inverse transfer function $S(\boldsymbol{\omega})$. In order to alleviate this deficiency, one can make the parameterization *adaptive* by using a set of the scale parameters. Although unexplored in this study, such adaptive modeling constitutes an important direction for a future research, since it is expected to noticeably increase the estimation quality, as well as to reduce its complexity.

An additional contribution in this work is in demonstrating the connection between the proposed inverse filtering and some nonblind deconvolution methods. Specifically, it was shown that the Fourier phase of estimated inverse filters can be used for recovering the related PSF, which can, in turn, be used for deconvolving the ultrasound images in a

nonblind manner. In this case, it is possible to further improve the deconvolution quality in terms of its computational efficiency and resolution gain.

In this paper, we have also provided some theoretical insights concerning the notion of sparse representation of tissue reflectivity functions. We demonstrated that the assumption of "sparse tissue" plays a crucial role in convergence of the "hybrid" inverse filter to its optimal form as defined by the correct value of its spectral phase. However, due to the linearity of this method, it was shown to be incapable of providing sparse reconstructions *per se*, as it forced the estimates to be devoid of high frequencies due to the effect of regularization. On the other hand, truly sparse solutions were obtained by means of the MAP deconvolution under Laplacian priors (see Section VII-A2). Due to its highly nonlinear nature, the latter was capable of interpolating the high frequencies of the reflectivity function, which were lost in the process of image formation.

Finally, a number of interesting research questions prompted by this study should be outlined. First, it is tempting to establish a firm theoretical basis underpinning the compact parametrization of the inverse filters using the notion of shift-invariant subspaces. Conditions and criteria should be defined with which one could predict the properties of the approximating subspace given, e.g., an observed PSF. Moreover, the present study focused on the application of the inverse filtering of the "hybrid" type to the problem of deconvolution of ultrasound images. However, we believe that this method can be applied to signals acquired by different imaging modalities. A demonstration of such applications deserves a separate study as well.

Acknowledgments

The authors would like to thank all the anonymous reviewers whose useful comments and suggestions have allowed substantially improving the quality of the present contribution.

This work was supported in part by the Natural Science and Engineering Research Council of Canada (NSERC) under a Discovery Grant, and in part by grants from the National Science Foundation, the Air Force Office of Sponsored Research, the Army Research Office, MURI, and MRI-HEL, as well as as by the National Institutes of Health under Grant NAC P41 RR-13218 through the Brigham and Women's Hospital. This work is part of the National Alliance for Medical Image Computing (NAMIC), supported by the National Institutes of Health through the NIH Roadmap for Medical Research, Grant U54 EB005149. Information on the National Centers for Biomedical Computing can be obtained from http://nihroadmap.nih.gov/bioinformatics. The associate editor coordinating the review of this manuscript and approving it for publication was Dr. Srdjan Stankovic.

Biography

Oleg Michailovich (M'02) was born in Saratov, Russia, in 1972. He received the M.Sc. degree in electrical engineering from the Saratov State University in 1994 and the M.Sc. and Ph.D. degrees in biomedical engineering from The Technion—Israel Institute of Technology, Haifa, in 2003.

He is currently with the Department of Electrical and Computer Engineering, University of Waterloo, Waterloo, ON, Canada. His research interests include the application of image

processing to various problems of image reconstruction, segmentation, inverse problems, nonparametric estimations, approximation theory, and multiresolution analysis.

Allen Tannenbaum (M'93) was born in New York in 1953. He received the Ph.D. degree in mathematics from Harvard University, Cambridge, MA, in 1976.

He has held faculty positions at the Weizmann Institute of Science, Rehovot, Israel; McGill University, Montreal, QC, Canda; ETH, Zurich, Switzerland; The Technion—Israel Institute of Technology, Haifa; the Ben-Gurion University of the Negev, Israel; and the University of Minnesota, Minneapolis. He is presently the Julian Hightower Professor of Electrical and Biomedical Engineering, Georgia Institute of Technology, Atlanta, and Emory University, Atlanta. He has done research in image processing, medical imaging, computer vision, robust control, systems theory, robotics, semiconductor process control, operator theory, functional analysis, cryptography, algebraic geometry, and invariant theory.

References

[1]. Hundt EE, Trautenberg EA. Digital processing of ultrasonic data by deconvolution. IEEE Trans. Son. Ultrason. Sep; 1980 SU-27(5):249–252.

[2]. Vollmann W. Resolution enhancement of ultrasonic B-scan images by deconvolution. IEEE Trans. Son. Ultrason. Mar; 1982 SU-29(2):78–83.

[3]. Iracà D, Landini L, Verrazzani L. Power spectrum equalization for ultrasonic image restoration. IEEE Trans. Ultrason., Ferroelect., Freq. Control. Mar; 1989 36(2):216–222.

[4]. Jensen JA, Mathorne J, Gravesen T, Stage B. Deconvolution of in vivo ultrasound B-mode images. Ultrason. Imag. Apr; 1993 15(2):122–133.

[5]. Abeyratne UR, Petropulu AP, Reid JM. Higher order spectra based deconvolution of ultrasound images. IEEE Trans. Ultrason., Ferroelect., Freq. Control. Nov; 1995 42(6):1064–1075.

[6]. Taxt T. Restoration of medical ultrasound images using two-dimensional homomorphic deconvolution. IEEE Trans. Ultrason., Ferroelect., Freq. Control. Jul; 1995 42(4):543–554.

[7]. Michailovich O, Adam D. A novel approach to the 2-D blind deconvolution problem in medical ultrasound. IEEE Trans. Med. Imag. Jan; 2005 24(1):86–104.

[8]. Angelsen, B. Ultrasound Imaging: Waves, Signals, and Signal Processing. Emantec; Trondhejm, Norway: 2000.

[9]. Cloostermans M, Thijssen J. A beam corrected estimation of the frequency dependent attenuation of biological tissues from backscattered ultrasound. Ultrason. Imag. Apr; 1983 5(2):136–147.

[10]. Narayana P, Ophir J, Maklad N. The attenuation of ultrasound in biological fluids. J. Acoust. Soc. Amer. Jul; 1984 76(1):1–4. [PubMed: 6747101]

[11]. Wear KA. The effects of frequency-dependent attenuation and dispersion on sound speed measurements: Application in human trabecular bone. IEEE Trans. Ultrason., Ferroelect., Freq. Control. Jan; 2000 47(1):265–273.

[12]. Haykin, S. Blind Deconvolution. Prentice-Hall; Englewood Cliffs, NJ: 1994.

[13]. Nagy J, O'Leary D. Restoring images degraded by spatially variant blur. SIAM J. Sci. Comput. Jul; 1998 19(4):1063–1082.

[14]. Oppenheim, AV.; Schafer, RW. Discrete Time Signal Processing. Prentice-Hall; London, U.K.: 1989.

[15]. Taxt T. Comparison of cepstrum-based methods for radial blind deconvolution of ultrasound images. IEEE Trans. Ultrason., Ferroelect., Freq. Control. May; 1997 44(3):666–674.

[16]. Jensen JA, Leeman S. Nonparametric estimation of ultrasound pulses. IEEE Trans. Biomed. Eng. Nov; 1994 41(10):929–936. [PubMed: 7959799]

[17]. Michailovich O, Adam D. Robust estimation of ultrasound pulses using outlier-resistant de-noising. IEEE Trans. Med. Imag. Mar; 2003 22(3):368–392.

[18]. Strand J, Taxt T, Jain AK. Two-dimensional phase unwrapping using a block least-squares method. IEEE Trans. Image Process. Mar; 1999 8(3):375–386. [PubMed: 18262880]

[19]. Ghiglia, DC.; Pritt, MD. Two-Dimensional Phase Unwrapping: Theory, Algorithms, and Software. Wiley; New York: 1998.

[20]. Tribolet JM. A new phase unwrapping algorithm. IEEE Trans. Acoust., Speech, Signal Process. Apr; 1977 ASSP-25(2):170–177.

[21]. Michailovich O, Adam D. Phase unwrapping for 2-D blind deconvolution of ultrasound images. IEEE Trans. Med. Imag. Jan; 2004 23(1):7–25.

[22]. Michailovich O, Tannenbaum A. A fast approximation of smooth functions from samples of partial derivatives with application to phase unwrapping. Signal Process. to be published.

[23]. Kundur D, Hatzinakos D. Blind image deconvolution. IEEE Signal Process. Mag. May; 1996 13(3):43–64.

[24]. Cadzow JA. Blind deconvolution via cumulant extrema. IEEE Signal Process. Mag. May; 1996 13(3):24–42.

[25]. de Boor C, Ron A. Fourier analysis of the approximation power of principal shift-invariant spaces. Constr. Approx. 1992; 8:427–462.

[26]. Ron, A. Multivariate Approximation and Applications. Cambridge Univ. Press; Cambridge, MA: 2001. Introduction to shift-invariant spaces: Linear independence; p. 112-151.

[27]. Carlin, BP.; Louis, TA. Monographs on Statistics and Applied Probability. Vol. 69. Chapman & Hall; New York: 1996. Bayes and empirical Bayes methods for data analysis.

[28]. Kaaresen KF, Bolviken E. Blind deconvolution of ultrasonic traces accounting for pulse variance. IEEE Trans. Ultrason., Ferroelect., Freq. Control. May; 1999 46(3):564–574.

[29]. Taylor HL, Banks SC, McCoy JF. Deconvolution with ℓ_1 norm. Geophysics. Jan; 1979 44(1):39–52.

[30]. Zibulevsky M, Pearlmutter BA. Blind source separation by sparse decomposition in a signal dictionary. Neural Comput. Apr; 2001 13(4):863–882. [PubMed: 11255573]

[31]. Chen, S.; Donoho, D. Atomic decomposition by basis pursuit; presented at the SPIE Int. Conf. Wavelets; San Diego, CA. Jul. 1995;

[32]. Hyvarinen, JKA.; Oja, E. Independent Component Analysis. Wiley; New York: 2001.

[33]. Stark, H. Image Recovery: Theory and Applications. Academic; New York: 1987.

[34]. Bronstein MM, Bronstein AM, Zibulevsky M, Zeevi YY. Blind deconvolution of images using optimal sparse representations. IEEE Trans. Image Process. Jun; 2005 14(6):726–736. [PubMed: 15971772]

[35]. Donoho, D. On minimum entropy deconvolution. 1981. [Online]. Available: http://www-stat.stanford.edu/donoho/Reports/Oldies/index.html [Online]. Available

[36]. Wiggins RA. Minimum entropy deconvolution. Geoexploration. 1978; 16:21–35.

[37]. Sekko E, Thomas G, Boukrouche A. A deconvolution technique using optimal wiener filtering and regularization. Signal Process. Jan; 1999 72(1):23–32.

[38]. Barva, M.; Kybic, J.; Mari, J-M.; Cachard, C.; Hlavac, V. Automatic localization of curvilinear object in 3D ultrasound images. In: Walker, WF.; Emelianov, SY., editors. Ultrasonic Imaging and Signal Processing, ser. Progress in Biomedical Optics and Imaging. Vol. 5750. SPIE; Bellingham, WA: Jul. 2005 p. 455-462.

[39]. Strang G, Fix G. A fourier analysis of the finite element variational method. Constr. Aspects Function Anal. 1973:793–840. C.I.M.E. II Ciclo 1971.

[40]. Tikhonov AN. On the stability of inverse problems. Dokl. Akad. Nauk SSSR. 1943; 39(5):195–198.

[41]. Michailovich, O.; Tannenbaum, A. A novel approach to the blind-deconvolution problem based on MAP optimality and sparsity constraints; presented at the IASTED SIP; Honolulu, HI. 2006;

[42]. Bertsekas, D. Nonlinear Programming. Athena Scientific; Belmont, MA: 1999.

[43]. Unser M, Aldroubi A, Eden M. B-spline signal processing: Part I - theory. IEEE Trans. Signal Process. Feb.1993 41(2>)

[44]. Unser M, Aldroubi A, Eden M. B-spline signal processing: Part II—efficient design and applications. IEEE Trans. Signal Process. Feb.1993 41(2)

[45]. Hansen, PC. SIAM, ser. Numerical Aspects of Linear Inversion. 1998. Rank-deficient and discrete ill-posed problems.

[46]. Dembo R, Steihaug T. Truncated-Newton algorithms for large-scale unconstrained optimization. Math. Progr. Jun.1983 26:190–212.

[47]. Boyd, S.; Vandenberghe, L. Convex Optimization. Cambridge Univ. Press; Cambridge, MA: 2004.

[48]. Donoho DL. De-noising by soft-thresholding. IEEE Trans. Inf. Theory. May; 1995 41(3):613–627.

[49]. Daubechies, I. SIAM. 1992. Ten lectures on wavelets.

[50]. Duan, Q.; Angelini, E.; Song, T.; Laine, A. Fast interpolation algorithms for real-time three-dimensional cardiac ultrasound; Proc. 25th Annu. Int. Conf. IEEE EMBS; 2003; p. 1192-1195.

[51]. Roggemann, MC.; Welsh, BM. Imaging Through Turbulence. CRC; Boca Raton, FL: 1996.

[52]. Jirik R, Taxt T. Two-dimensional blind iterative deconvolution of medical ultrasound images. Proc. IEEE Ultrasonics Symp. Aug.2004 2:1262–1265.

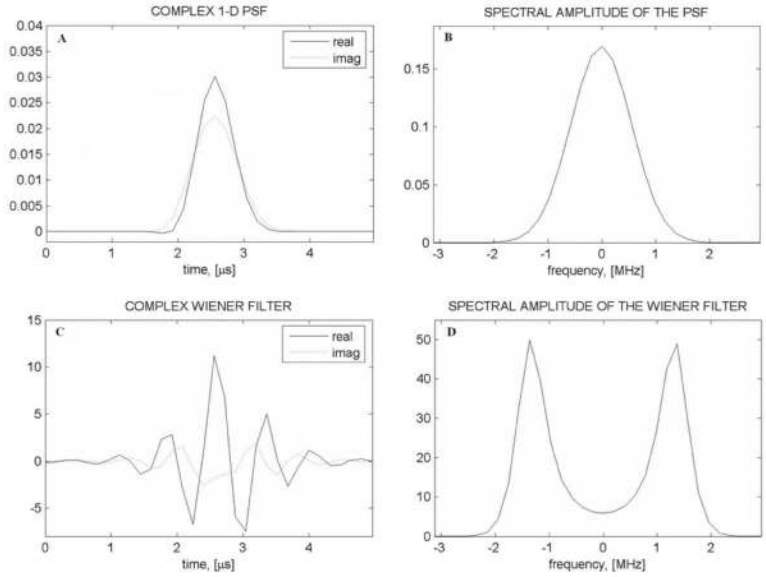

Fig. 1.

(A) (solid line) Real and (dotted line) imaginary parts of a measured 1-D PSF; (B) amplitude of the DFT of the PSF; (C) corresponding Wiener filter as defined by (15) for $\varepsilon = 10^{-4}$; (D) amplitude of the DFT of the Wiener filter.

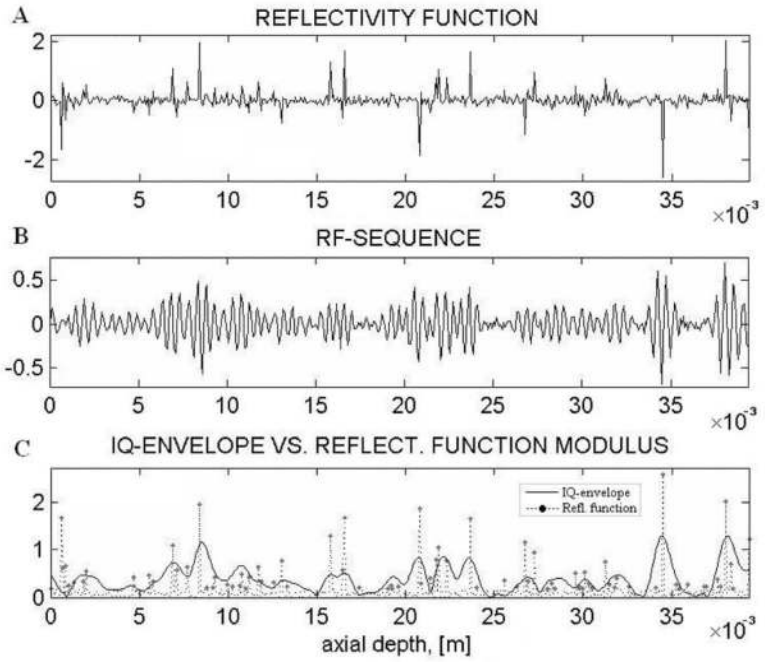

Fig. 2.

(A) Example of the reflectivity function used in the *in silico* experiments of Section VIII-A; (B) corresponding RF-sequence; (C) magnitude of (solid line) the corresponding IQ-sequence versus (dotted line) the absolute value of the reflectivity function.

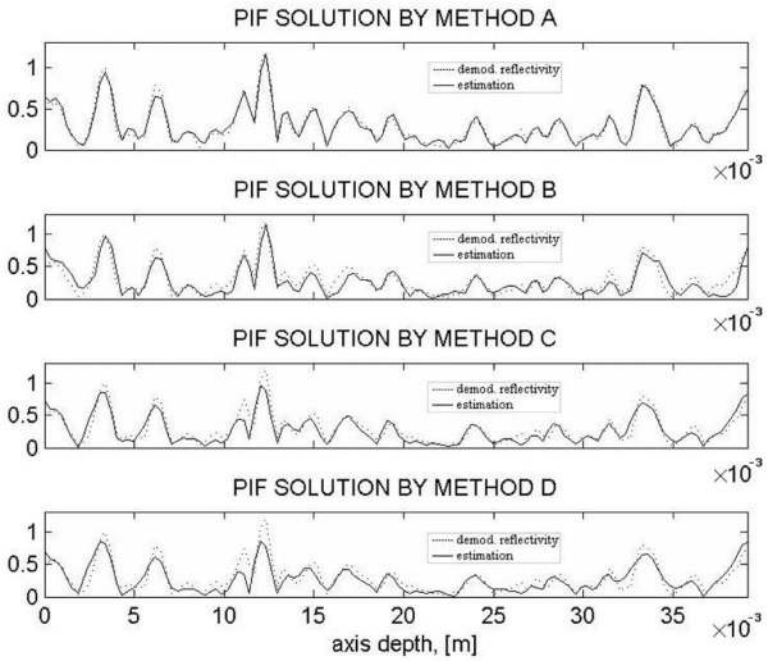

Fig. 3.

(From top to bottom) IQ sequences deconvolved using the "Hybrid-Spline," "Hybrid-Fourier," "ML-Spline," and "ML-Fourier" methods. (Dotted line) Note that all the estimates are shown together with the corresponding demodulated reflectivity function.

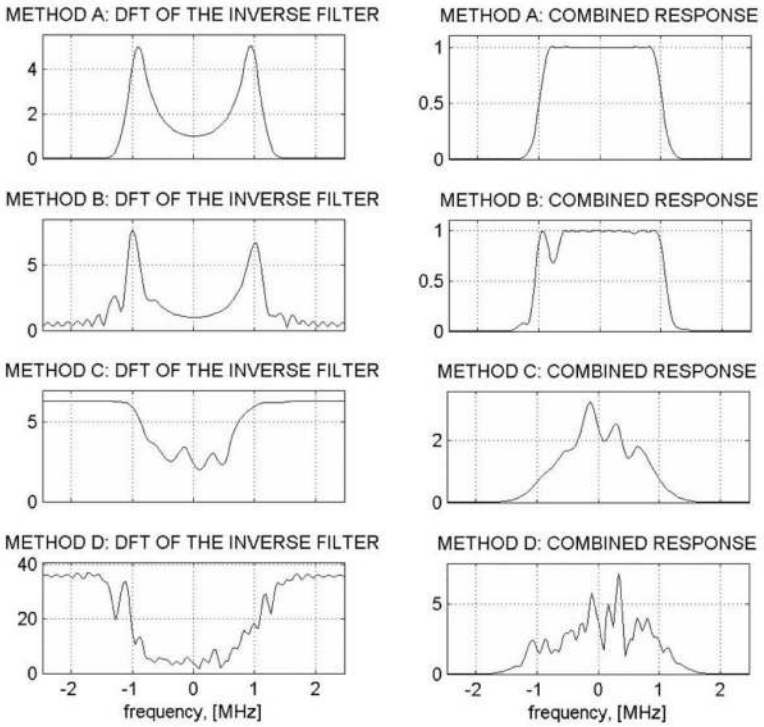

Fig. 4.

(Left column) DFT magnitude $S(\omega)$ of the inverse filters computed by [from top to bottom] the "Hybrid-Spline," "Hybrid-Fourier," "ML-Spline," and "ML-Fourier" methods. (Right column) DFT magnitude of the combined response $H(\omega)\ S(\omega)$ corresponding to [from top to bottom] the "Hybrid-Spline," "Hybrid-Fourier," "ML-Spline," and "ML-Fourier" methods.

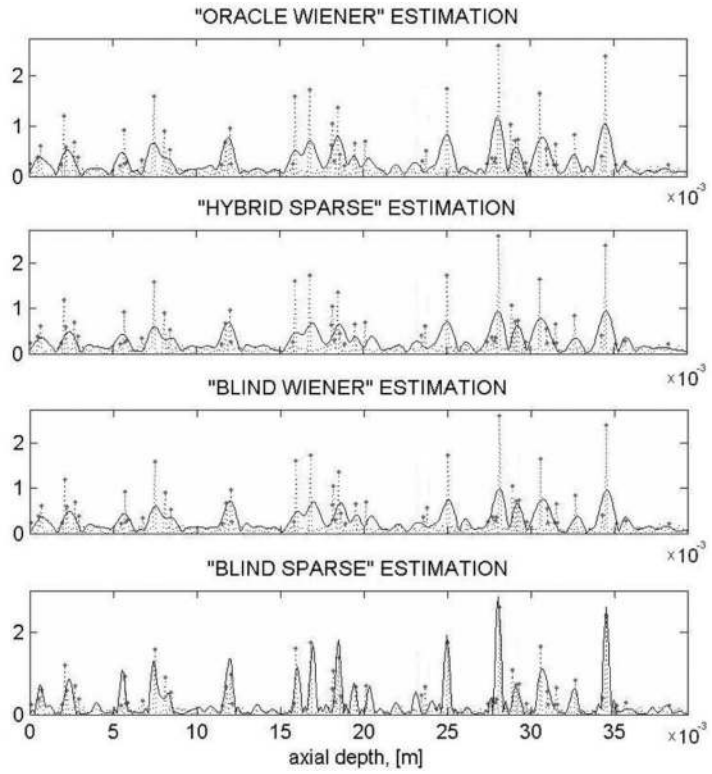

Fig. 5.
(Solid lines) Estimates of the (dotted line) reflectivity function computed using (from top to bottom) the “Oracle Wiener,” “Hybrid-Spline,” “Blind Wiener,” and “Blind Sparse” deconvolution methods.

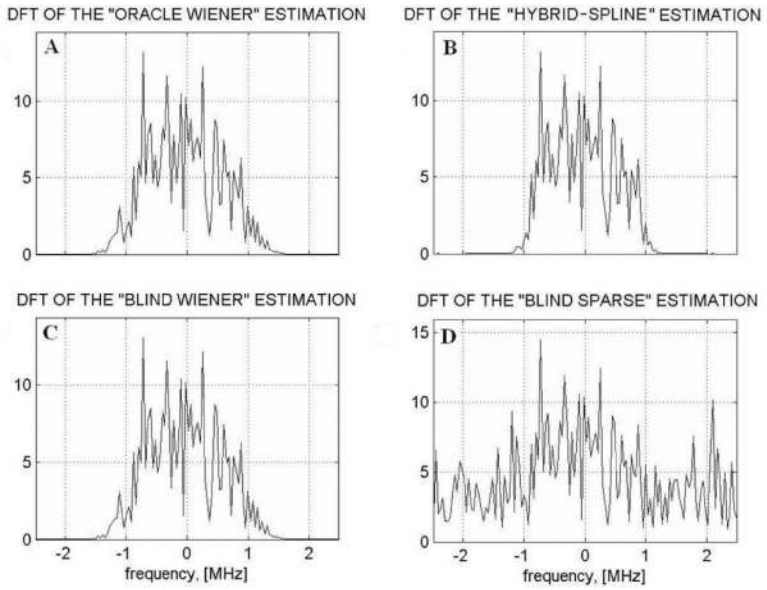

Fig. 6.

(A)–(D) Magnitude of the DFT of the estimates shown Fig. 5(A)–(D), in the same order.

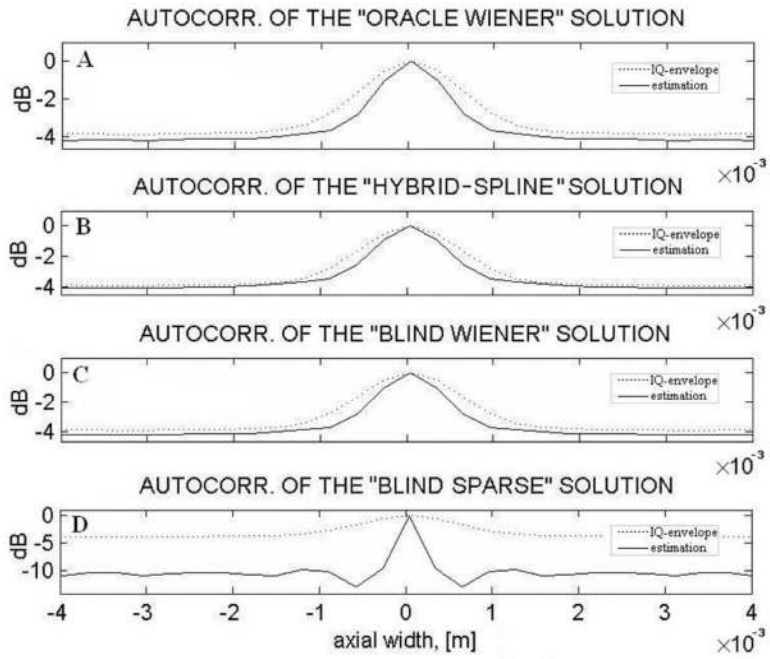

Fig. 7.

(A) Autocorrelation function of the “Oracle Wiener” estimates; (B) auto-correlation function of the “Hybrid-Spline” estimates; (C) autocorrelation function of the “Blind Wiener” estimates; (D) autocorrelation function of the “Blind Sparse” estimates. Note that all these autocorrelation functions have been computed by ensemble-averaging the results of 100 independent trials.

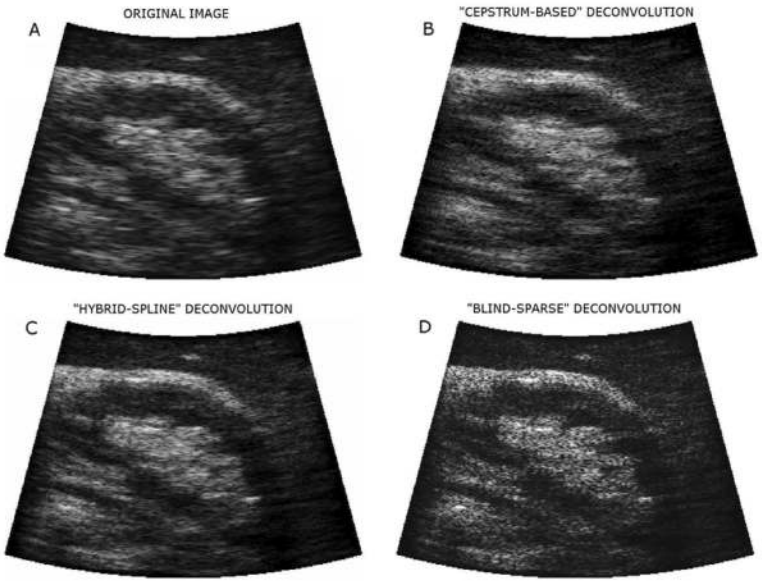

Fig. 8.

(A) Fragment of the original image of a right kidney; (B) reconstruction by the “cepstrum-based” deconvolution method of [6]; (C) reconstruction by the “Hybrid-Spline” method; (D) reconstruction by the “Blind-Sparse” method.

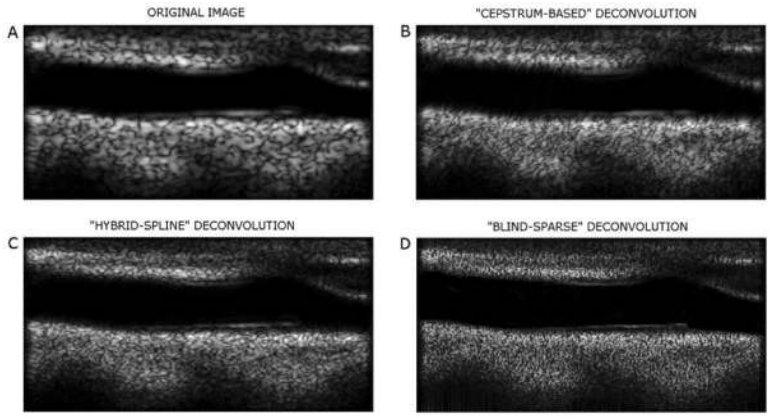

Fig. 9.

(A) Fragment of the original image of a carotid artery (longitudinal view); (B) reconstruction by the “cepstrum-based” deconvolution method; (C) reconstruction by the “Hybrid-Spline” method; (D) reconstruction by the “Blind-Sparse” method.

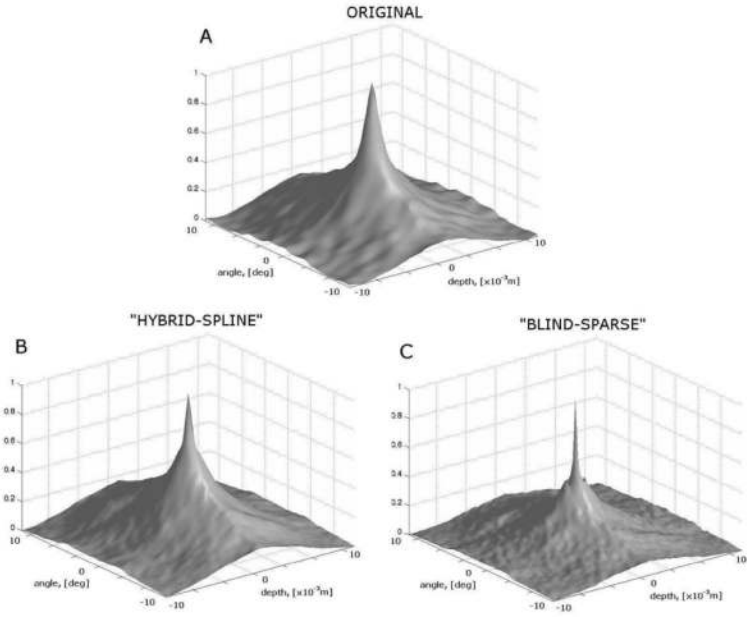

Fig. 10.

Autocorrelation functions of: (A) original images; (B) images reconstructed by the “Hybrid-Spline” method; (C) images reconstructed by the “Blind-Sparse” method.

TABLE I

NMSE ("Plus-Minus" Its Standard Deviation) Computed for the Original IQ-Envelope and the Estimates Obtained by the "Oracle Wiener," "Hybrid-Spline," "Hybrid-Fourier," "ML-Spline," and "ML-Fourier" Methods

	SNR=10 dB	**SNR=14 dB**	**SNR = 20 dB**
Original envelope	0.230 ± 0.036	0.120 ± 0.019	0.082 ± 0.012
"Oracle Wiener"	0.026 ± 0.008	0.013 ± 0.004	0.009 ± 0.003
"Hybrid-Spline"	0.031 ± 0.007	0.016 ± 0.004	0.011 ± 0.002
"Hybrid-Fourier"	0.101 ± 0.026	0.048 ±0.013	0.034 ± 0.009
"ML-Spline"	0.174 ± 0.058	0.082 ± 0.022	0.058 ± 0.013
"ML-Fourier"	0.222 ± 0.076	0.103 ± 0.035	0.076 ± 0.025

TABLE II

Average Values of the "Shift" Error, the Number of Iterations, and of the Duration of One Newton Iteration for the "Oracle Wiener," "Hybrid-Spline," "Hybrid-Fourier," "ML-Spline," "ML-Fourier" Deconvolution Methods

	"Shift" Error	Number of Iterations	Duration of One Iteration (msec)
"Hybrid-Spline"	0.00 ± 0.00	31.8 ± 4.0	10.8 ± 0.3
"Hybrid-Fourier"	3.21 ± 1.57	53.2 ± 8.7	15.0 ± 0.9
"ML-Spline"	0.01 ± 0.00	40.5 d= 5.7	13.2 ± 0.8
"ML-Fourier"	9.10 ± 4.03	137.8 ± 35.1	17.8 ± 0.9